

Universal Stabilization of a Parametrically Coupled Qubit

Yao Lu,^{1,*} S. Chakram,¹ N. Leung,¹ N. Earnest,¹ R. K. Naik,¹ Ziwen Huang,² Peter Groszkowski,² Eliot Kapit,³ Jens Koch,² and David I. Schuster^{1,†}

¹*The James Franck Institute and Department of Physics, University of Chicago, Chicago, Illinois 60637, USA*

²*Department of Physics and Astronomy, Northwestern University, Evanston, Illinois 60208, USA*

³*Department of Physics and Engineering Physics, Tulane University, New Orleans, Louisiana 70118, USA*

(Received 11 July 2017; published 13 October 2017)

We autonomously stabilize arbitrary states of a qubit through parametric modulation of the coupling between a fixed frequency qubit and resonator. The coupling modulation is achieved with a tunable coupling design, in which the qubit and the resonator are connected in parallel to a superconducting quantum interference device. This allows for quasistatic tuning of the qubit-cavity coupling strength from 12 MHz to more than 300 MHz. Additionally, the coupling can be dynamically modulated, allowing for single-photon exchange in 6 ns. Qubit coherence times exceeding 20 μ s are maintained over the majority of the range of tuning, limited primarily by the Purcell effect. The parametric stabilization technique realized using the tunable coupler involves engineering the qubit bath through a combination of photon nonconserving sideband interactions realized by flux modulation, and direct qubit Rabi driving. We demonstrate that the qubit can be stabilized to arbitrary states on the Bloch sphere with a worst-case fidelity exceeding 80%.

DOI: 10.1103/PhysRevLett.119.150502

Dissipation is generally thought of as competing with quantum coherence. However, under appropriate circumstances dissipation can be engineered and utilized as a resource for coherent quantum control [1–3]. Dissipation can be used to generate and stabilize entangled states [4,5] and many-body phases [6,7]. Quantum error correction, one of the main goals in quantum information science, can also be achieved by autonomously stabilizing a manifold of states [8–11] through bath engineering, without the need for active feedback. In superconducting circuit QED, engineered dissipation has been used in conjunction with the Josephson nonlinearity of the qubit to achieve stabilization of qubit [4,5,12–14] and cavity states [15,16], important steps towards autonomous error correction. A more convenient approach to quantum state stabilization, however, may lie in the direct modulation of the coupling between the system and a quantum bath, a task that can be accomplished by using tunable coupler devices [17–20].

Tunable coupling elements can mediate interactions while maintaining coherence. They have been used for frequency conversion [19,21] and quantum logic gates [18,20], and are suitable for a variety of tasks in quantum information processing [22,23] and quantum simulation [24]. In this Letter, we present a tunable coupling circuit in which a single-junction transmon is coupled to a dissipative bath in the form of a low- Q cavity, via grounding through a shared dc SQUID. We show that the coupling can be tuned over a large dynamic range using magnetic flux, with very little qubit dephasing from flux noise. By parametric modulation of the coupling, we realize both photon conserving red-sideband interactions to transfer single photons [25–27], as well as photon nonconserving blue-sideband interactions

[27–30] necessary for state stabilization. We present a scheme to parametrically stabilize arbitrary single-qubit states by using the blue-sideband interaction in conjunction with a regular qubit Rabi drive.

The tunable coupling circuit, shown in Fig. 1, consists of a transmon qubit [31] and a lumped-element resonator, both grounded at the same node through a dc SQUID. The dc SQUID acts as a tunable inductor shared between the qubit and the resonator, creating a coupling strength between the two systems proportional to its inductance $L_g = L_{g0}/|\cos(\pi\Phi_{\text{ext}}/\Phi_0)|$, which is controlled by the external flux Φ_{ext} threading the loop. Previous tunable coupler designs [18,20] utilized series coupling schemes that are convenient for chains and lattices of qubits or resonators. By contrast, the topology of our circuit enables many resonators or qubits to share the same coupler, which is suitable for random access memories [23]. The circuit is described by the effective Hamiltonian,

$$\hat{H} = \omega_r \hat{a}^\dagger \hat{a} + \frac{\omega_q}{2} \hat{\sigma}_z - g_R (\hat{a}^\dagger \hat{\sigma}^- + \hat{a} \hat{\sigma}^+) - g_B (\hat{a}^\dagger \hat{\sigma}^+ + \hat{a} \hat{\sigma}^-), \quad (1)$$

where

$$g_{R,B} = \frac{L_{g0}}{2|\cos(\pi\Phi_{\text{ext}}/\Phi_0)|} \sqrt{\frac{\omega_r \omega_q}{L_r L_q}} \mp \frac{C_g}{2} \sqrt{\frac{\omega_r \omega_q}{C_r C_q}} \quad (2)$$

are the coupling strengths associated with the red and blue sidebands [28]. The operators \hat{a} and $\hat{\sigma}^-$ represent the lowering operators for the cavity and the qubit mode, and ω_r , ω_q are the mode frequencies. The definitions of

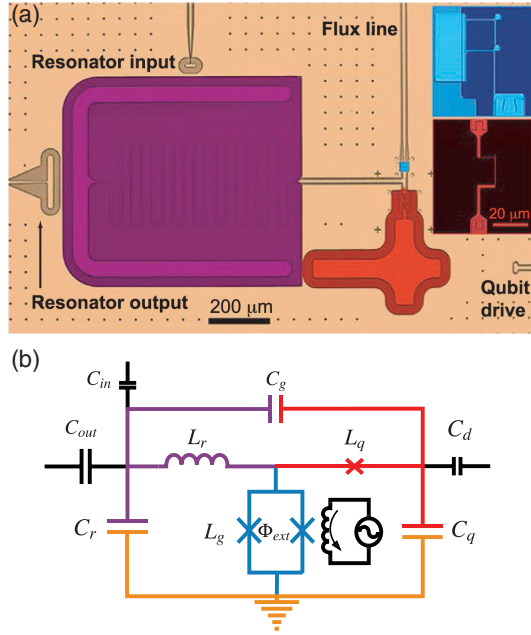


FIG. 1. (a) Optical image and (b) circuit diagram of our device. The lumped-element resonator is formed by a “C” shaped capacitor pad and an isolated meander line inductor. The inductor line protrudes to the common node where both the qubit Josephson junction and the coupler SQUID loop are connected. Two voltage ports are placed at the two sides of the resonator’s capacitor pad enabling transmission measurements. The qubit-cavity coupling strength is tuned with the SQUID-loop flux by modulating the current that flows through the flux line. The qubit can be probed via a separate qubit drive line that is weakly coupled to the qubit’s shunting capacitor. Insets show the details of the qubit Josephson junction and dc SQUID loop.

inductances and capacitances for qubit and resonator can be read off from Fig. 1(b). In the Hamiltonian above, the degree of freedom associated with the SQUID coupler has been adiabatically eliminated [32]. When the coupler is not being driven, the counter-rotating g_B term can usually be dropped from Eq. (1), but by dynamically modulating the inductance via the external flux Φ_{ext} , both red- and blue-sideband interactions can be utilized. Additionally, by balancing the inductive and capacitive terms in Eq. (2), one can make g_R 0 or even negative.

We perform spectroscopy of the qubit (Fig. 2) to determine the static coupling strength $g_R(\Phi_{\text{ext}})$, finding it to range from 12 to 300 MHz. The coupling strength is calculated from the size of photon-number splitting $2\chi = g_R^2 \alpha / \Delta(\Delta + \alpha)$ [31,40], where $\alpha = -188$ MHz is the qubit anharmonicity and Δ is the qubit-cavity detuning. At flux values where the splitting is too small to be resolved, we calibrate g_R by measuring the qubit Rabi rate through the cavity at fixed power [32]. As the qubit itself does not have a SQUID loop, its frequency is only indirectly affected by the modulation of the coupler. We choose $L_{q0} \ll L_r, L_q$ to ensure that the tuning of the qubit and resonator frequencies

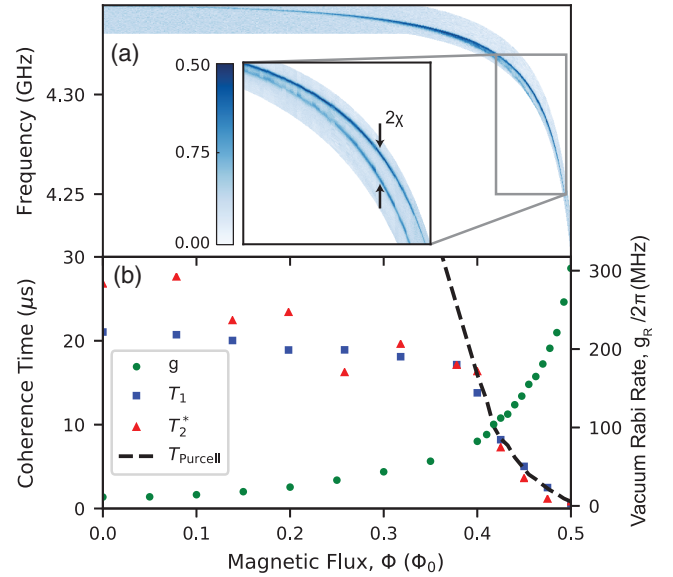


FIG. 2. (a) Spectroscopy showing the qubit excited state population as a function of flux through the coupler. The qubit frequency is insensitive over nearly the entire flux range. (Inset) Number splitting of the qubit peak due to photons in the resonator, used to calibrate the static coupling between the qubit and the resonator. (b) Qubit coherence and qubit-cavity coupling strength as a function of the flux through the coupler. The dephasing time (T_2^*) is comparable to the energy relaxation time (T_1) over the entire tuning range. The coherence times drop near $\Phi = 0.5\Phi_0$ as a result of the Purcell effect due to the strong coupling to the readout resonator, as indicated by the black dashed line.

from the change in the coupler inductance is small. As seen in Fig. 2, the qubit frequency varies by less than 15 MHz over 80% of the tuning range, making the qubit nearly immune to flux noise. Both the energy relaxation time T_1 and the dephasing time T_2^* remain above 20 μs over most of the flux period ($|\Phi_{\text{ext}}| < 0.4\Phi_0$). Only when the flux approaches half a flux quantum do coherence times start to drop significantly. There the Purcell effect from coupling to the readout resonator, as well as an increased frequency-flux sensitivity, limits the coherence.

The usefulness of parametric coupling becomes most evident when the qubit-cavity coupling strength is modulated at the qubit-cavity difference or sum frequency. Modulation of Φ_{ext} in Eq. (2) at frequency ω_d turns $g_{R,B}$ into $g_{R,B}(t) = \sum_n g_{R,B}^{(n)} \cos(\omega_d^{(n)} t)$, where $\omega_d^{(n)} = n\omega_d$ is the effective modulation frequency of the n th harmonic with Fourier coefficient $g_{R,B}^{(n)}$. Substituting this into Eq. (1), we obtain the red- and blue-sideband Hamiltonians in rotating frames as

$$\hat{H}_{\text{rot}}^{R,B} = (\omega_r' \mp \omega_q' - \chi' \hat{\sigma}_z) \hat{a}^\dagger \hat{a} \pm \frac{\omega_d}{2} \hat{\sigma}_z - g_{R,B}' (\hat{a}^\dagger \hat{\sigma}^\mp + \hat{a} \hat{\sigma}^\pm), \quad (3)$$

valid for effective modulation frequencies, $\omega_d^{(n)} \approx \omega_r' \pm (\omega_q' + \chi')$, respectively, with fast-oscillating terms

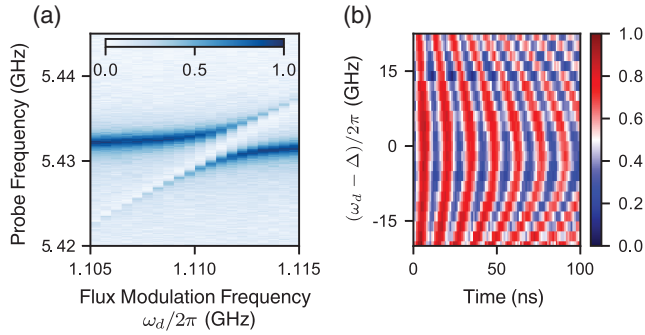


FIG. 3. Red-sideband interactions probed by applying a rf flux tone to the tunable coupler to generate sidebands. (a) Spectroscopy of the (normalized) resonator transmission as a function of sideband and resonator probe frequency, showing the stimulated vacuum Rabi spitting. (b) Stimulated vacuum Rabi oscillations between the qubit and resonator, measured as an oscillation of the qubit excited state population. A single photon is loaded into the qubit before the flux pulse.

abandoned. Here, the primes stand for the dressed basis after diagonalizing the static component of the driven Hamiltonian. At $\omega_d^{(n)} = \omega'_r - \omega'_q + \chi'$, energy pumped into the circuit through the parametric flux drive bridges the gap between the first excited state of the qubit $|e0\rangle$ and the single-photon Fock state of the cavity $|g1\rangle$, causing a splitting of $2g'_R$ due to the red-sideband coupling between the two levels. This is seen as an avoided crossing in the cavity transmission spectrum when the modulation frequency matches the detuning [Fig. 3(a)]. In the time domain, the red-sideband coupling mediates stimulated vacuum Rabi oscillations that coherently swap a single photon between qubit and resonator. The oscillation rate, $2g'_R/2\pi \approx 80$ MHz, can be directly seen from Fig. 3(b) and determines how fast qubit-photon gates can be performed.

While the red-sideband coupling enables photon-conserving processes, the blue-sideband coupling, which takes place at $\omega_d^{(n)} = \omega'_r + \omega'_q - \chi'$, generates two-photon oscillations between states $|g0\rangle$ and $|e1\rangle$. This interaction, created in our experiment through the second harmonic term by flux modulating at $\omega_d = (\omega'_r + \omega'_q - \chi')/2$, produces a much richer resonance structure in transmission [Fig. 4(a)], which can be accurately reproduced numerically [Fig. 4(b)]. The observed features can be understood conceptually by considering the energy level diagram in the rotating frame [Fig. 4(c)]. The blue-sideband interaction acts as a coherent two-photon pump that drives the circuit to $|e1\rangle$, causing an avoided crossing between $|g0\rangle$ and $|e1\rangle$ in the level diagram. As the cavity photon loss rate is faster than the qubit decay rate by 2 orders of magnitude in the experiment ($1/\kappa \approx 100$ ns and $T_1 > 20$ μ s), $|e1\rangle \rightarrow |e0\rangle$ is the dominant decay process and traps most of the population in the single-photon subspace in state $|e0\rangle$. When both photons are eventually lost from the circuit, the state immediately transitions to $|e1\rangle$, beginning the cycle again.

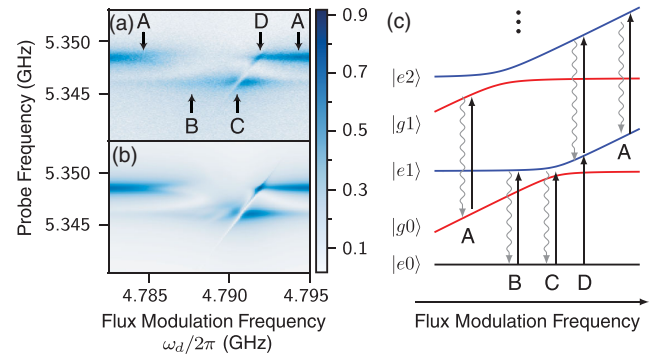


FIG. 4. Resonator spectroscopy showing (normalized) transmission near the blue-sideband resonance condition. Experimental data (a) and master equation simulations (b) show excellent agreement. (c) The energy level diagram corresponding to Eq. (3) provides a map to the spectroscopic features A, B, C, and D at different modulation frequencies, indicated by arrows in (a). A: When the modulation frequency is far detuned from the blue-sideband resonance, the qubit stays in its ground state. B: The excited state of the qubit is stabilized, causing the cavity to be shifted down by 2χ . C: The crossing of $|e1\rangle$ and $|g0\rangle$, manifest as an avoided crossing. The qubit excited state is also maximally stabilized at this frequency due to the resonance of $|e1\rangle$ and $|g0\rangle$. D: Enhanced cavity transmission appears when $|e0\rangle \rightarrow |g0\rangle$ and $|g0\rangle \rightarrow |g1\rangle$ transition energies are equal. The asymmetry of the unshifted cavity peak line centered at the blue-sideband resonance is likely due to interactions between higher levels $|g, n\rangle \rightarrow |e, n+1\rangle$.

In this sense, the blue-sideband flux drive stabilizes the qubit in the excited state. This, in turn, shifts the cavity frequency down by $2\chi'$ [B in Fig. 4(a)]. Furthermore, as the blue-sideband interaction splits the degenerate levels of $|e1\rangle$ and $|g0\rangle$ in the rotating frame, the cavity transmission measurement actually probes the transitions between $|e0\rangle$ and $(|e1\rangle \pm |g0\rangle)/\sqrt{2}$ so that the avoided crossing is visible within the shifted cavity peak [C in Fig. 4(a)]. Enhanced cavity transmission is observed at the crossing between the unshifted cavity peak and the avoided crossing [D in Fig. 4(a)]. Here the transition energy between $|e0\rangle$ and $|g0\rangle$ in the rotating frame coincides with the energy between $|g0\rangle$ and $|g1\rangle$, resulting in an enhanced transmission due to the $|g0\rangle$ population being weakly replenished by the cavity probe.

With the blue-sideband coupling being a critical component, we show that it is possible to take a further step towards stabilizing arbitrary states on the Bloch sphere with our tunable coupler circuit. Analogous to coherent population trapping [41,42] but using a harmonic oscillator as the dissipative element, the system is driven with both blue-sideband modulation and qubit Rabi drive at detunings and strengths as shown in Fig. 5(a).

Qubit states are dressed by the Rabi drive to become $|\tilde{g}\rangle = \cos(\theta/2)|g\rangle - e^{i\phi}\sin(\theta/2)|e\rangle$ and $|\tilde{e}\rangle = \sin(\theta/2)|g\rangle + e^{i\phi}\cos(\theta/2)|e\rangle$ in the rotating frame [Fig. 5(b)], where the

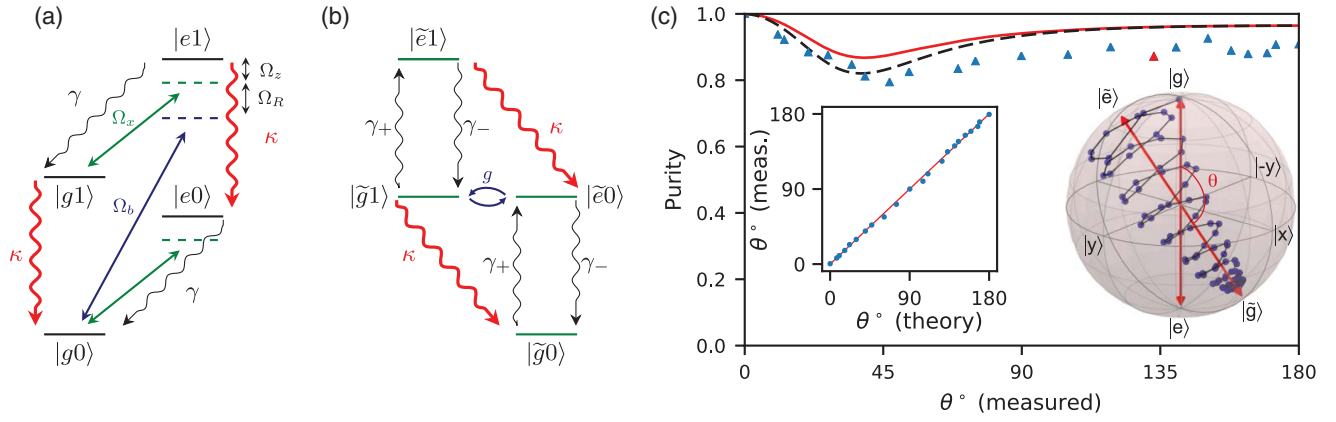


FIG. 5. Illustration of the universal stabilization scheme for single-qubit states. In the lab frame (a), qubit Rabi drive and blue-sideband modulation are applied with appropriately chosen detuning and strength. In the rotating frame (b), these two drives result in the dressing of the qubit state into arbitrary superpositions $|\tilde{g}\rangle$, $|\tilde{e}\rangle$, with resonant coupling between $|\tilde{e}0\rangle$ and $|\tilde{g}1\rangle$. Together with the aid of the fast cavity decay, these finally lead to the stabilization of the $|\tilde{g}0\rangle$ state. (c) The stabilization purity $|\langle\vec{\sigma}\rangle|$, plotted against the polar angle θ of the stabilization axis, both obtained from qubit tomography. Purities exceeding 80% are achieved over the entire Bloch sphere, while purities $> 90\%$ and $> 99\%$ are reached for stabilizing the $|e\rangle$ ($\theta = 180^\circ$) and $|g\rangle$ ($\theta = 0^\circ$) states, respectively. Experimental data qualitatively agree with the analytical calculation from Eq. (5) (red line) and numerical master equation simulation (black dashed line). The stabilization experiment was performed at zero flux, where qubit and cavity frequencies are $\omega_q/2\pi = 4.343$ GHz and $\omega_r/2\pi = 5.439$ GHz, with the linewidths being $\gamma/2\pi \approx 7.6$ kHz, $\gamma_\phi/2\pi \approx 3$ kHz, and $\kappa/2\pi \approx 1.6$ MHz. Left inset: stabilization angles predicted by theory closely match the experimental values. Right inset: trajectory of the qubit state in the dynamic process of stabilization, for the specific case of $\theta = 135^\circ$ (red triangle) with measured purity of 87%. Starting from $|g\rangle$, the qubit state moves in a helical path along the stabilization axis, until it saturates around the rotating frame ground state, $|\tilde{g}\rangle$.

polar angle $\theta = \arccos(\Omega_z/\Omega_R)$ is defined by the Rabi drive detuning Ω_z and the total Rabi frequency $\Omega_R = \sqrt{\Omega_x^2 + \Omega_z^2}$, while the azimuthal angle ϕ is determined by the phase of the Rabi drive. The dressing of the qubit states also leads to modified decay and excitation rates between $|\tilde{g}\rangle$ and $|\tilde{e}\rangle$ [Fig. 5(b)]. These can be found by rewriting the master equation dissipators in the dressed basis as

$$\tilde{\gamma}_- = \gamma \cos^4 \frac{\theta}{2} + \frac{\gamma_\phi}{2} \sin^2 \theta, \quad \tilde{\gamma}_+ = \gamma \sin^4 \frac{\theta}{2} + \frac{\gamma_\phi}{2} \sin^2 \theta, \quad (4)$$

where γ and γ_ϕ stand for the qubit decay and dephasing rate in the zero-temperature lab frame [32].

The blue-sideband drive with amplitude Ω_b provides a resonant interaction of strength $g = \Omega_b \sin^2(\theta/2)$ between the rotating frame states $|\tilde{g}1\rangle$ and $|\tilde{e}0\rangle$. Along with the fast decay of the resonator, this interaction yields an effective transition rate $\Gamma = 4g^2\kappa/(\kappa^2 + 4g^2)$ among qubit states $|\tilde{e}\rangle$ and $|\tilde{g}\rangle$. This produces an overall qubit decay rate of $\tilde{\gamma}_- + \Gamma$ that competes against the excitation rate $\tilde{\gamma}_+$, to stabilize the effective ground state $|\tilde{g}\rangle$ with a population of

$$P_{\tilde{g}} = \frac{\gamma_- + \Gamma}{\gamma_- + \gamma_+ + \Gamma}. \quad (5)$$

As both polar and azimuthal angles of $|\tilde{g}\rangle$ can be easily manipulated in the experiment, this scheme allows for stabilization along an arbitrary direction with high fidelity.

We apply this protocol to demonstrate stabilization of arbitrary states on the Bloch sphere. The polar angle was varied by changing the Rabi drive detuning Ω_z while keeping its strength $\Omega_x/2\pi$ fixed at 9 MHz. As can be seen from Eq. (5), the azimuthal angle has no effect on the stabilization fidelity and was thus set to 0. The amplitude of the flux modulation is calibrated to create a constant blue-sideband coupling strength $\Omega_b/2\pi = 0.5$ MHz for all stabilization angles, with the detuning chosen in each case to be $\Omega_z + \Omega_R$. The measured stabilization purity $|\langle\vec{\sigma}\rangle| = \sqrt{\langle\sigma_x\rangle^2 + \langle\sigma_y\rangle^2 + \langle\sigma_z\rangle^2}$ is plotted as a function of the stabilization polar angle θ in Fig. 5(c), which closely follows the theory prediction made by Eq. (5). The excited state $|e\rangle$ is stabilized with 93% purity at $\theta = 180^\circ$, where only the blue-sideband process is required. Purity starts to reduce as θ is lowered, which can be understood by the blue-sideband interaction losing efficiency in coupling the $|\tilde{g}1\rangle$ and $|\tilde{e}0\rangle$ states when the rotating-frame ground state $|\tilde{g}\rangle$ has less overlap with the bare excited state, $|e\rangle$. This, however, does not invalidate the scheme's performance for small angles. According to Eq. (4), the qubit's natural decay guarantees $\tilde{\gamma}_- \gg \tilde{\gamma}_+$ as $\theta \rightarrow 0$, resulting in good stabilization fidelity in Eq. (5), irrespective of how small Γ is. This is reflected in Fig. 5(c) as a revival of the purity from a minimum value of $\sim 80\%$ to near unity (limited by lab-frame qubit temperature) at $\theta = 0$, where the lab-frame ground state $|g\rangle$ is stabilized through the natural decay of the qubit. The high fidelity at all stabilization angles

therefore relies upon the mixed contribution of the active stabilization process induced by the blue-sideband interaction (Γ), and the passive process from natural qubit decay ($\tilde{\gamma}_-$).

In summary, we have demonstrated a cavity-assisted, autonomous protocol for universal qubit state stabilization, an important step towards stabilization of many-body states [6,7] and autonomous error correction [8,9,11]. The circuit developed in this work provides a flux-controlled tunable coupling between two fixed frequency modes, and maintains excellent coherence over the majority of the tuning range. In addition to stabilization, the circuit is capable of producing red-sideband interactions, critical for frequency conversion, random access gates, and quantum communication. Finally, a single tunable coupler can support several modes, significantly reducing the complexity of large quantum circuits and their associated room-temperature electronics.

We thank M. W. Wei, Andy C. Y. Li, D. C. McKay, and J. Lawrence for helpful discussions. Research was sponsored by the Army Research Laboratory and was accomplished under Cooperative Grant No. W911NF-15-2-0058. The views and conclusions contained in this document are those of the authors and should not be interpreted as representing the official policies, either expressed or implied, of the Army Research Laboratory or the U.S. Government. The U.S. Government is authorized to reproduce and distribute reprints for government purposes notwithstanding any copyright notation herein. Research was also supported by the U.S. Department of Defense (DOD) under DOD Contract No. H98230-15-C0453. Use of the Center for Nanoscale Materials, an Office of Science user facility, was supported by the U.S. Department of Energy, Office of Science, Office of Basic Energy Sciences, under Award No. DE-AC02-06CH11357. This work made use of the Pritzker Nanofabrication Facility of the Institute for Molecular Engineering at the University of Chicago, which receives support from SHyNE, a node of the National Science Foundation's National Nanotechnology Coordinated Infrastructure (Grant No. NSF NNCI-1542205). E. K. was supported by the Louisiana Board of Regents Grant No. LEQSF(2016-19)-RD-A-19 and by the National Science Foundation Grant No. PHY-1653820. We gratefully acknowledge support from the David and Lucile Packard Foundation.

*luy100@uchicago.edu

†David.Schuster@uchicago.edu

- [1] D. J. Wineland and W. M. Itano, *Phys. Today* **40**, 34 (1987).
- [2] J. F. Poyatos, J. I. Cirac, and P. Zoller, *Phys. Rev. Lett.* **77**, 4728 (1996).
- [3] V. Vuletić and S. Chu, *Phys. Rev. Lett.* **84**, 3787 (2000).
- [4] S. Shankar, M. Hatridge, Z. Leghtas, K. M. Sliwa, A. Narla, U. Vool, S. M. Girvin, L. Frunzio, M. Mirrahimi, and M. H. Devoret, *Nature (London)* **504**, 419 (2013).

- [5] S. Hacoheh-Gourgy, V. V. Ramasesh, C. De Grandi, I. Siddiqi, and S. M. Girvin, *Phys. Rev. Lett.* **115**, 240501 (2015).
- [6] R. Ma, C. Owens, A. Houck, D. I. Schuster, and J. Simon, *Phys. Rev. A* **95**, 043811 (2017).
- [7] B. M. Anderson, R. Ma, C. Owens, D. I. Schuster, and J. Simon, *Phys. Rev. X* **6**, 041043 (2016).
- [8] Z. Leghtas, G. Kirchmair, B. Vlastakis, R. J. Schoelkopf, M. H. Devoret, and M. Mirrahimi, *Phys. Rev. Lett.* **111**, 120501 (2013).
- [9] E. Kapit, J. T. Chalker, and S. H. Simon, *Phys. Rev. A* **91**, 062324 (2015).
- [10] E. Kapit, *Phys. Rev. A* **92**, 012302 (2015).
- [11] E. Kapit, *Phys. Rev. Lett.* **116**, 150501 (2016).
- [12] P. J. Leek, S. Filipp, P. Maurer, M. Baur, R. Bianchetti, J. M. Fink, M. Göppl, L. Steffen, and A. Wallraff, *Phys. Rev. B* **79**, 180511 (2009).
- [13] K. W. Murch, U. Vool, D. Zhou, S. J. Weber, S. M. Girvin, and I. Siddiqi, *Phys. Rev. Lett.* **109**, 183602 (2012).
- [14] M. E. Kimchi-Schwartz, L. Martin, E. Flurin, C. Aron, M. Kulkarni, H. E. Tureci, and I. Siddiqi, *Phys. Rev. Lett.* **116**, 240503 (2016).
- [15] Z. Leghtas, S. Touzard, I. M. Pop, A. Kou, B. Vlastakis, A. Petrenko, K. M. Sliwa, A. Narla, S. Shankar, M. J. Hatridge *et al.*, *Science* **347**, 853 (2015).
- [16] E. T. Holland, B. Vlastakis, R. W. Heeres, M. J. Reagor, U. Vool, Z. Leghtas, L. Frunzio, G. Kirchmair, M. H. Devoret, M. Mirrahimi *et al.*, *Phys. Rev. Lett.* **115**, 180501 (2015).
- [17] M. Allman, J. Whittaker, M. Castellanos-Beltran, K. Cicak, F. da Silva, M. DeFeo, F. Lecocq, A. Sirois, J. Teufel, J. Aumentado *et al.*, *Phys. Rev. Lett.* **112**, 123601 (2014).
- [18] Y. Chen, C. Neill, P. Roushan, N. Leung, M. Fang, R. Barends, J. Kelly, B. Campbell, Z. Chen, B. Chiaro *et al.*, *Phys. Rev. Lett.* **113**, 220502 (2014).
- [19] A. J. Sirois, M. A. Castellanos-Beltran, M. P. DeFeo, L. Ranzani, F. Lecocq, R. W. Simmonds, J. D. Teufel, and J. Aumentado, *Appl. Phys. Lett.* **106**, 172603 (2015).
- [20] D. C. McKay, S. Filipp, A. Mezzacapo, E. Magesan, J. M. Chow, and J. M. Gambetta, *Phys. Rev. Applied* **6**, 064007 (2016).
- [21] E. Zakka-Bajjani, F. Nguyen, M. Lee, L. R. Vale, R. W. Simmonds, and J. Aumentado, *Nat. Phys.* **7**, 599 (2011).
- [22] N. Didier, J. Bourassa, and A. Blais, *Phys. Rev. Lett.* **115**, 203601 (2015).
- [23] R. K. Naik, N. Leung, S. Chakram, P. Groszkowski, Y. Lu, N. Earnest, D. C. McKay, J. Koch, and D. I. Schuster, *arXiv:1705.00579*.
- [24] P. Roushan, C. Neill, A. Megrant, Y. Chen, R. Babbush, R. Barends, B. Campbell, Z. Chen, B. Chiaro, A. Dunsworth *et al.*, *Nat. Phys.* **13**, 146 (2016).
- [25] F. Beaudoin, M. P. da Silva, Z. Dutton, and A. Blais, *Phys. Rev. A* **86**, 022305 (2012).
- [26] J. D. Strand, M. Ware, F. Beaudoin, T. A. Ohki, B. R. Johnson, A. Blais, and B. L. T. Plourde, *Phys. Rev. B* **87**, 220505 (2013).
- [27] M. Roth, M. Ganzhorn, N. Moll, S. Filipp, G. Salis, and S. Schmidt, *arXiv:1708.02090*.
- [28] A. Wallraff, D. I. Schuster, A. Blais, J. M. Gambetta, J. Schreier, L. Frunzio, M. H. Devoret, S. M. Girvin, and R. J. Schoelkopf, *Phys. Rev. Lett.* **99**, 050501 (2007).

- [29] P. J. Leek, S. Filipp, P. Maurer, M. Baur, R. Bianchetti, J. M. Fink, M. Göppl, L. Steffen, and A. Wallraff, *Phys. Rev. B* **79**, 180511 (2009).
- [30] S. Novikov, T. Sweeney, J. E. Robinson, S. P. Premaratne, B. Suri, F. C. Wellstood, and B. S. Palmer, *Nat. Phys.* **12**, 75 (2015).
- [31] J. Koch, T. M. Yu, J. Gambetta, A. A. Houck, D. I. Schuster, J. Majer, A. Blais, M. H. Devoret, S. M. Girvin, and R. J. Schoelkopf, *Phys. Rev. A* **76**, 042319 (2007).
- [32] See Supplemental Material <http://link.aps.org/supplemental/10.1103/PhysRevLett.119.150502> for more information, which includes Refs. [33–39].
- [33] C. Song, M. P. DeFeo, K. Yu, and B. L. T. Plourde, *Appl. Phys. Lett.* **95**, 232501 (2009).
- [34] S. Gladchenko, D. Olaya, E. Dupont-Ferrier, B. Douçot, L. B. Ioffe, and M. E. Gershenson, *Nat. Phys.* **5**, 48 (2009).
- [35] K. Fossheim and A. Sudbø, *Superconductivity: Physics and Applications* (John Wiley & Sons, Ltd., Chichester, 2005).
- [36] A. D. Córcoles, J. M. Chow, J. M. Gambetta, C. Rigetti, J. R. Rozen, G. A. Keefe, M. B. Rothwell, M. B. Ketchen, and M. Steffen, *Appl. Phys. Lett.* **99**, 181906 (2011).
- [37] A. Wallraff, D. I. Schuster, A. Blais, L. Frunzio, J. Majer, M. H. Devoret, S. M. Girvin, and R. J. Schoelkopf, *Phys. Rev. Lett.* **95**, 060501 (2005).
- [38] E. Kapit, M. Hafezi, and S. H. Simon, *Phys. Rev. X* **4**, 031039 (2014).
- [39] A. A. Clerk, M. H. Devoret, S. M. Girvin, F. Marquardt, and R. J. Schoelkopf, *Rev. Mod. Phys.* **82**, 1155 (2010).
- [40] D. I. Schuster, A. A. Houck, J. A. Schreier, A. Wallraff, J. M. Gambetta, A. Blais, L. Frunzio, J. Majer, B. Johnson, M. H. Devoret *et al.*, *Nature (London)* **445**, 515 (2007).
- [41] B. Dalton, R. McDuff, and P. Knight, *Opt. Acta* **32**, 61 (1985).
- [42] E. Arimondo, *Prog. Opt.* **35**, 257 (1996).